

An optimized approach toward high energy density cathode material for K-ion batteries



Ji Ung Choi^a, Yun Ji Park^a, Jae Hyeon Jo^a, Young Hwa Jung^b, Do-Cheon Ahn^b, Tae-Yeol Jeon^b,
Kug-Seung Lee^b, Hyungsub Kim^c, Seongsu Lee^c, Jongsoon Kim^{a,**}, Seung-Taek Myung^{a,*}

^a Department of Nanotechnology and Advanced Materials Engineering & Sejong Battery Institute, Sejong University, Seoul, 05006, South Korea

^b Beamline Department, Pohang Accelerator Laboratory (PAL), Pohang, 37673, South Korea

^c Korea Atomic Energy Research Institute (KAERI), Daejeon, 34507, South Korea

ARTICLE INFO

Keywords:

Layered
Potassium
Cathode
Battery
First-principles calculation

ABSTRACT

Herein, we propose P'2-K_x[Ni_{0.05}Mn_{0.95}]O₂ as a promising cathode material for high-energy-density potassium-ion batteries (KIBs). The P'2-K_{0.83}[Ni_{0.05}Mn_{0.95}]O₂ delivers a high discharge capacity of 155 mAh g⁻¹ (52 mA g⁻¹) as well as a high energy density of 420 Wh kg⁻¹ in the voltage range of 1.5–4.3 V. Surprisingly, the fast K-ion migration in the P'2-K_{0.83}[Ni_{0.05}Mn_{0.95}]O₂ structure with a low activation barrier energy of ~271 meV enables achievement of high capacity at high currents, 78 mAh g⁻¹ at 2600 mA g⁻¹, as well as long-term cycling stability with capacity retention of ~77% after 500 cycles at 520 mA g⁻¹. *Operando* synchrotron X-ray diffraction analysis reveals that P'2-K_{0.83}[Ni_{0.05}Mn_{0.95}]O₂ retains the P'2-phase without P'2-OP4 phase transition during charge/discharge in the voltage range of 1.5–4.3 V, which is abnormal compared to the other P'2-based layered cathode materials for sodium-ion batteries, being responsible for the long-term cycle stability of P'2-K_{0.83}[Ni_{0.05}Mn_{0.95}]O₂. First-principles calculation results indicate that the excellent electrochemical performance results from the structural stability associated with a single -phase reaction upon K⁺ extraction/insertion out of/into the host structure. The remarkable potassium storage capability of P'2-K_{0.83}[Ni_{0.05}Mn_{0.95}]O₂ makes it a promising cathode candidate for KIBs.

1. Introduction

Over the past several decades, Li-ion batteries (LIBs) have been considered to be the best energy storage devices because of their high energy density [1,2]. However, their use is limited for large-scale applications owing to the recent surge in the cost of lithium resources [3]. Recently, potassium-ion batteries (KIBs) have emerged as an alternatives to LIBs because of the relative abundance of potassium resources (2.09 wt % of the Earth's crust) relative to that of lithium reserves (only 0.0017 wt %) [4] as well as the similar chemistries of KIBs and LIBs [5,6]. Several types of cathode materials for KIBs have been investigated including Prussian blue analogues [7–9], polyanionic compounds [10,11], organic materials [12,13], and layered oxides [14–17]. Although the large size of potassium ions (1.38 Å) as charge carriers relative to that of lithium ions (0.76 Å) impedes their facile diffusion into the host structure, the similarity in the resulting electrochemical reaction upon insertion has stimulated the exploration of promising high-capacity cathode materials for

KIBs.

The aforementioned representative cathode materials have remarkable features. Prussian blue analogues have an open metal-organic-framework structure, which provides not only high capacity and operation voltage but also readiness for reversible potassium-ion intercalation [9]. Na superionic conductor (NASICON) polyanionic compounds possess thermal stability with an acceptable level of capacity. Nevertheless, the crystal structure of has not yet been identified [18]. The structural flexibility of organic compounds enables accommodation of large potassium ions and molecules [9]. Finally, layered oxides such as P2- and P3-K_xMeO₂ (Me: transition metal) are of interest because of their high capacities, delivering ~120 mAh g⁻¹ in the voltage range of 1.5–3.9 V [15,16]. Raising the upper voltage cutoff is challenging because of the P3-O3 phase transition as well the electrolyte instability at high voltage [19]. With these issues in mind, we aimed to design a Mn-based layered oxide as a high-energy-density cathode material. As research on Na–Mn–O compounds has shown that P'2-Na_{0.67}MnO₂ and its derivatives

* Corresponding author.

** Corresponding author.

E-mail addresses: jongsoonkim@sejong.ac.kr (J. Kim), smyung@sejong.ac.kr (S.-T. Myung).

<https://doi.org/10.1016/j.ensm.2020.02.025>

Received 11 November 2019; Received in revised form 25 December 2019; Accepted 23 February 2020

Available online 25 February 2020

2405-8297/© 2020 Elsevier B.V. All rights reserved.

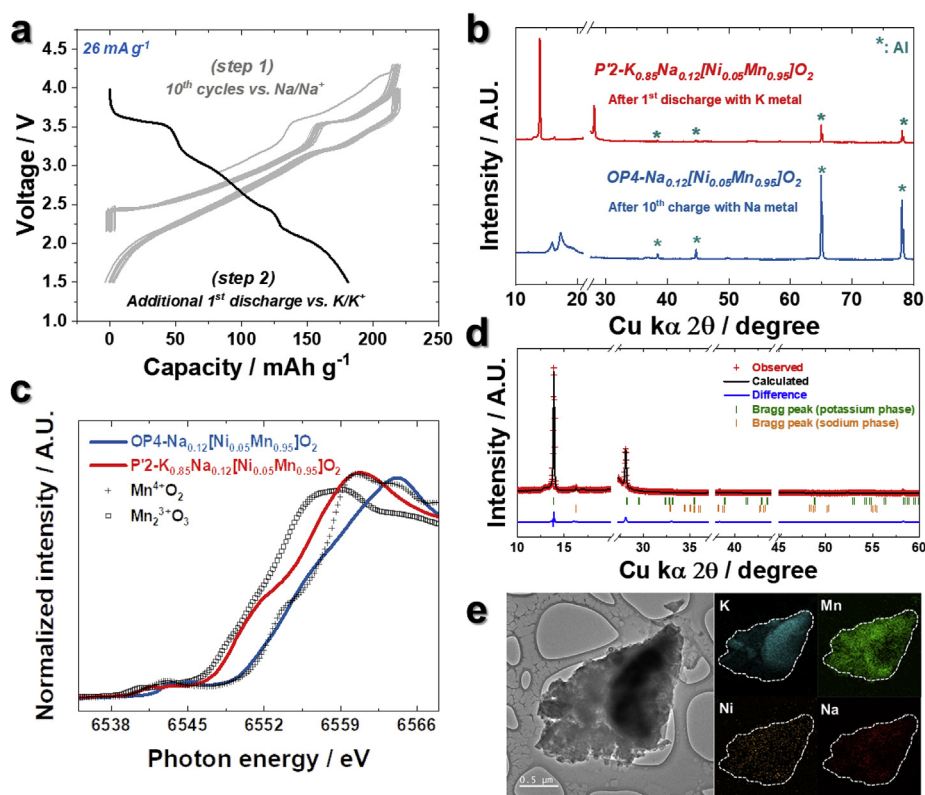


Fig. 1. (a) Charge–discharge curves for the operating voltage range of 1.5–4.3 V; grey color (step 1) denotes cycling done in a Na cell to establish Na⁺ diffusion path, and black color (step 2) illustrates the first insertion of K⁺ into Na_{0.12}[Ni_{0.05}Mn_{0.95}]O₂, which resulted in K_{0.85}Na_{0.12}[Ni_{0.05}Mn_{0.95}]O₂, (b) XRD patterns of OP4–Na_{0.12}[Ni_{0.05}Mn_{0.95}]O₂ after 10th charge in a Na cell (bottom) and P'2–K_{0.85}Na_{0.12}[Ni_{0.05}Mn_{0.95}]O₂ after first insertion of K⁺ into Na_{0.12}[Ni_{0.05}Mn_{0.95}]O₂, (c) XANES spectra of Mn K-edge for 10th desodiated electrode and 1st potassiated electrode, (d) Rietveld refinement result with Mylar film: 17°–30°, and (e) TEM–EDS mapping image for 1st potassiated electrode. (For interpretation of the references to color in this figure legend, the reader is referred to the Web version of this article.)

[20–22], which have a distorted P2 structure that elongates the *b*-axis in the unit cell, can tolerate the phase transition from continuous P'2 to OP4 phases.

Herein, we propose a new promising cathode material, P'2–K_{0.83}[Ni_{0.05}Mn_{0.95}]O₂, for use in KIBs. P'2–Na_{0.67}[Ni_{0.05}Mn_{0.95}]O₂ was selected as the starting material for electrochemical ion exchange of Na⁺ to K⁺ ions in K cells. The ion exchange appears to be an efficient process, as the crystal structure is not altered owing to the similarity of the ionic radii of Na⁺ (1.02 Å) and K⁺ (1.37 Å). Thus, a fully desodiated P'2–Na_{0.12}[Ni_{0.05}Mn_{0.95}]O₂ electrode was subjected to cycling in K cells to extract the remaining Na ions in the structure, which yielded the formation of P'2–K_{0.83}[Ni_{0.05}Mn_{0.95}]O₂. Indeed, it is possible to potassiate sodiated cathode materials with K metal as the counterpart as previously

reported P3–K_{0.69}CrO₂ [14] and P2–K_{2/3}[Ni_{1/3}Mn_{2/3}]O₂ [23]. However, the deposition of Na metal onto K metal produces a Na–K alloy, which is a liquid state like mercury, is extremely flammable and causes explosion in presence of air [24]. For the reason, we removed sodium ion in Na cells as much as we can in order to minimize the side effect induced by the formation of Na–K alloy on the surface of K metal, which deteriorates the cell performances that was proved by Goodenough et al. [25] and Zhang et al. [26]. This motivated us to insert potassium ions after the 10th desodiation.

The proposed P'2–K_{0.83}[Ni_{0.05}Mn_{0.95}]O₂ cathode delivered high discharge capacities; namely, 155 mAh g⁻¹ (420 Wh kg⁻¹) at a current of 52 mA g⁻¹ with capacity retention of 83% for 200 cycles and 120 mAh g⁻¹ at a current of 520 mA g⁻¹ with capacity retention of 77% for 500

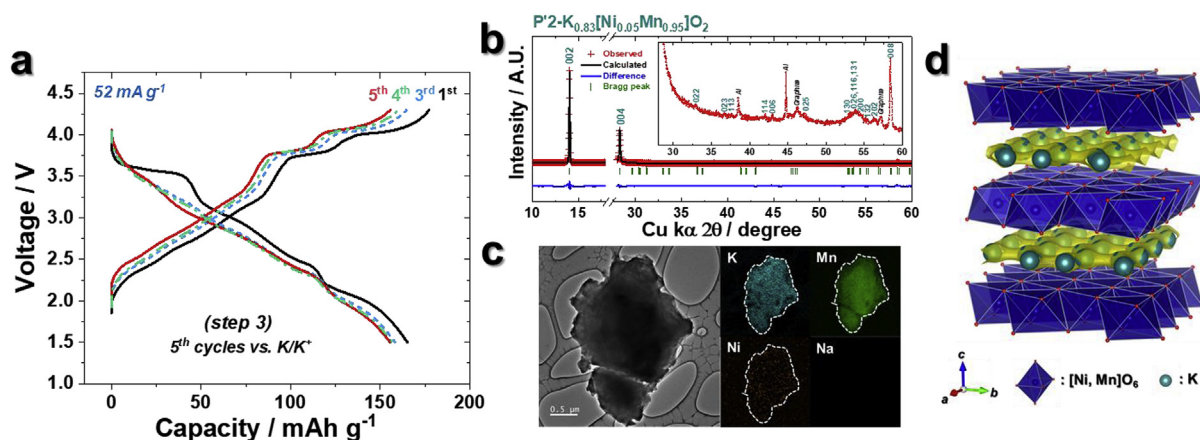


Fig. 2. Formation process for P'2–K_{0.83}[Ni_{0.05}Mn_{0.95}]O₂. (a) Charge–discharge curves for the operating voltage range of 1.5–4.3 V, (b) Rietveld refinement result of XRD data for K_{0.83}[Ni_{0.05}Mn_{0.95}]O₂ obtained after five cycles of Na_{0.12}[Ni_{0.05}Mn_{0.95}]O₂, namely, formation process, in a K cell; Mylar film: 17°–30° (inset: XRD pattern at 29°–60°), (c) TEM and EDS mapping image of P'2–K_{0.83}[Ni_{0.05}Mn_{0.95}]O₂ electrode, (d) BVS energy landscape of P'2–K_xNi_{0.05}Mn_{0.95}O₂ that predicts possible K⁺ atomic sites and diffusion paths.

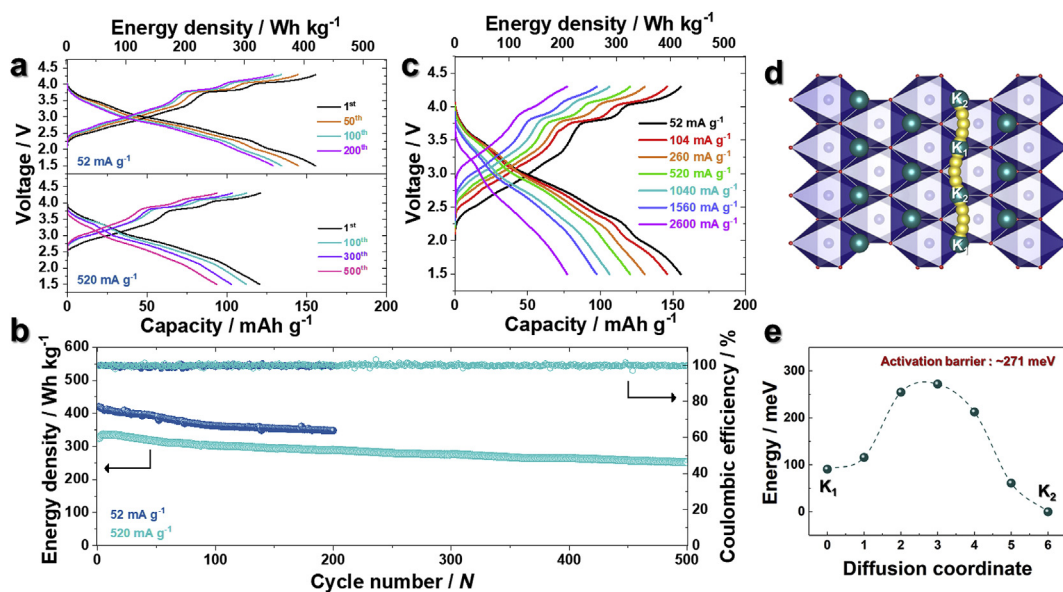


Fig. 3. (a) Charge–discharge curves for $K_{0.83}[Ni_{0.05}Mn_{0.95}]O_2$ tested in the operating voltage range of 1.5–4.3 V, (b) the corresponding cycling performance, (c) voltage curves tested at various currents (52, 104, 260, 520, 1040, 1560, and 2600 $mA\ g^{-1}$), (d) K^+ ionic diffusion motion and (e) activation barrier energy in $P'2-K_x[Ni_{0.05}Mn_{0.95}]O_2$ predicted by NEB method with first-principles calculation.

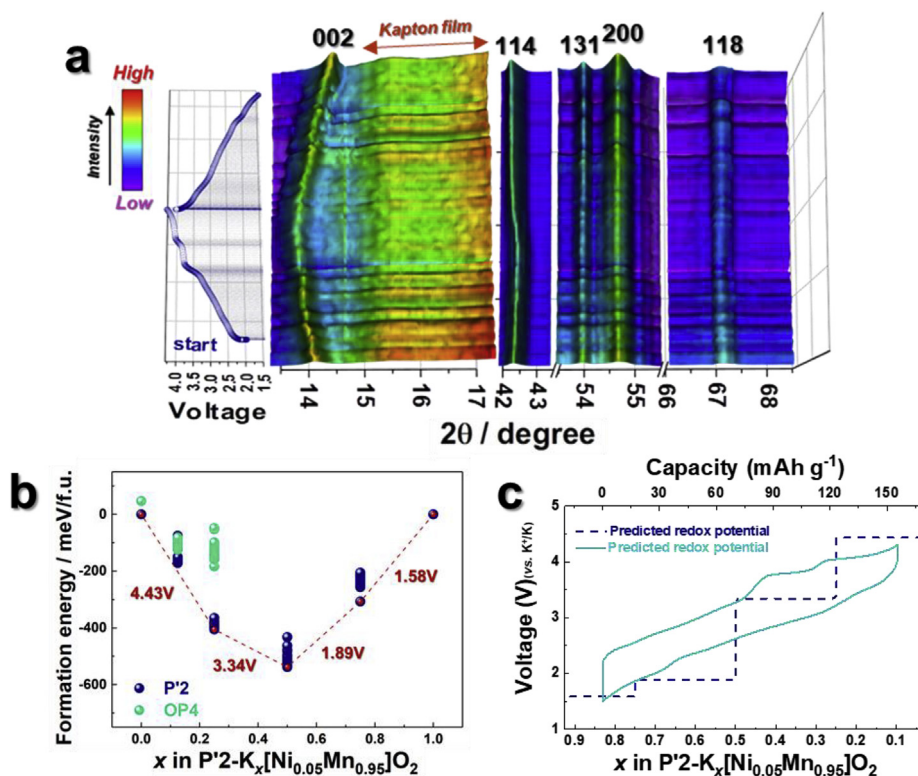


Fig. 4. (a) *Operando* synchrotron X-ray diffraction patterns of $K_{0.83}[Ni_{0.05}Mn_{0.95}]O_2$; Kapton film: 17° – 30° , (b) formation energies of $P'2/OP4-K_x[Ni_{0.05}Mn_{0.95}]O_2$ configurations ($0 \leq x \leq 1$) predicted by first-principles calculation, (c) comparison of experimentally measured charge/discharge curves and predicted voltage curves obtained using first-principles calculations.

cycles. First-principles calculation revealed that the migration of K ions in $P'2-K_x[Ni_{0.05}Mn_{0.95}]O_2$ has an activation energy barrier of ~ 271 meV, which is significantly lower than those of other layered transition metal oxides (typically > 500 meV) for sodium-ion batteries [27]. Interestingly, *operando* synchrotron X-ray diffraction study revealed that

$P'2-K_x[Ni_{0.05}Mn_{0.95}]O_2$ retained the original $P'2$ -based structure during charging to 4.3V (vs. K^+/K) without $P'2$ - $OP4$ phase transition, which is responsible for the outstanding cycle-performance despite charging to 4.3V (vs. K^+/K), as elucidated by first-principles calculations.

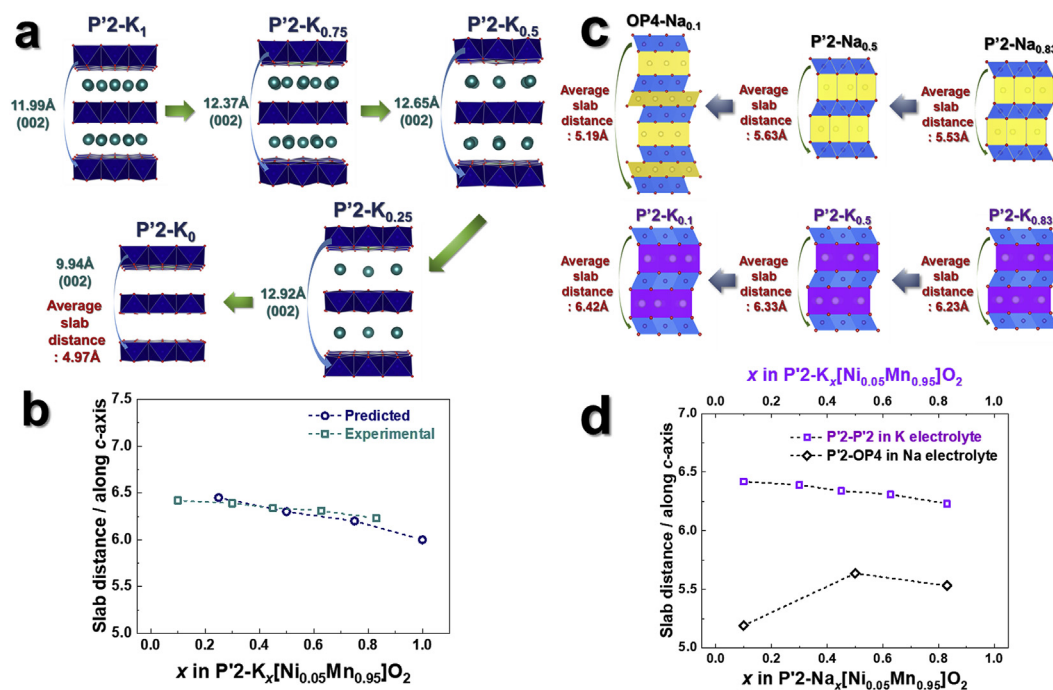


Fig. 5. (a) Predicted structural change of P'2-K_xNi_{0.05}Mn_{0.95}O₂ depending on K contents in the structure using first-principles calculation, (b) Change of the slab distances of P'2-K_x[Ni_{0.05}Mn_{0.95}]O₂ along c-axis determined using *operando* synchrotron XRD with Rietveld refinement and first-principles calculation. (c) Experimental structural change of P'2-K_xNi_{0.05}Mn_{0.95}O₂ and P'2-Na_xNi_{0.05}Mn_{0.95}O₂ (x = 0.1, 0.5, and 0.83) [20] depending on K and Na contents in the structure, (d) Comparison of change of the slab distances for P'2-K_x[Ni_{0.05}Mn_{0.95}]O₂ and P'2-Na_x[Ni_{0.05}Mn_{0.95}]O₂ along c-axis determined using *operando* synchrotron XRD with Rietveld refinement.

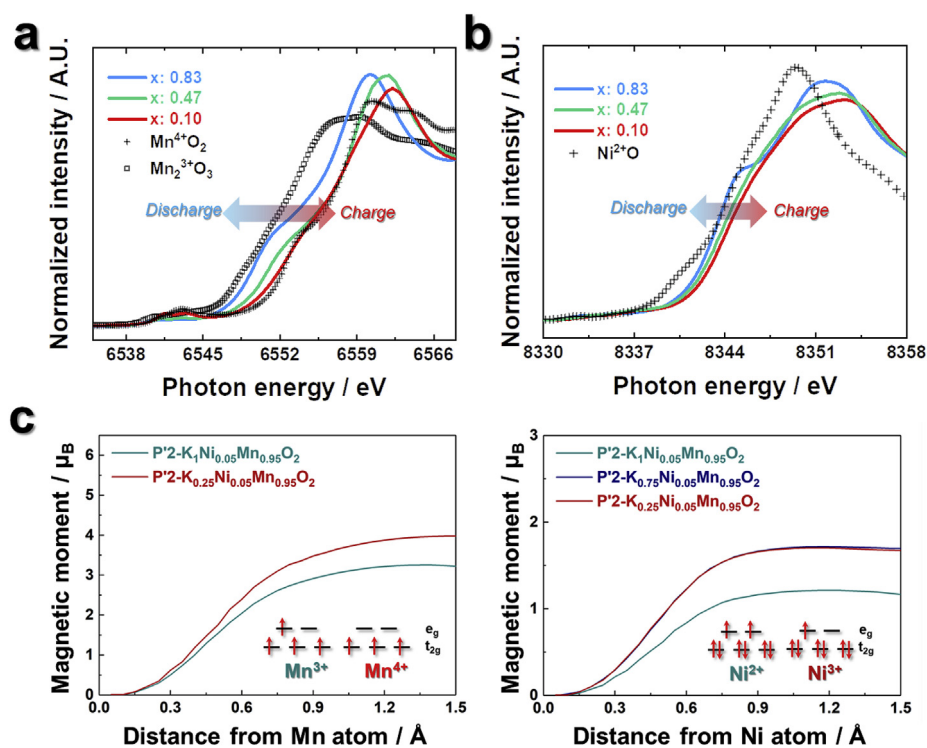


Fig. 6. XANES spectra of (a) Mn K-edge and (b) Ni K-edge for K_x[Ni_{0.05}Mn_{0.95}]O₂ (x = 0.1–0.83) electrodes. (c) Spin integration on Mn and Ni ions in P'2-K_x[Ni_{0.05}Mn_{0.95}]O₂.

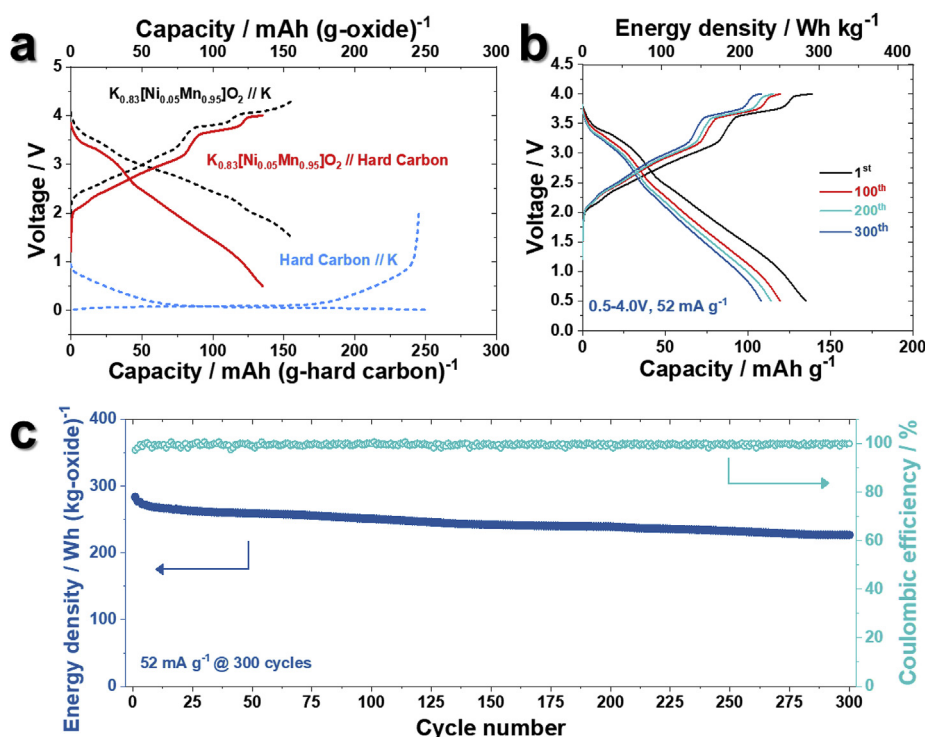


Fig. 7. (a) First charge-discharge curves of P'2- $\text{K}_{0.83}[\text{Ni}_{0.05}\text{Mn}_{0.95}]\text{O}_2//\text{K}$ metal (black), hard carbon//K metal (blue), P'2- $\text{K}_{0.83}[\text{Ni}_{0.05}\text{Mn}_{0.95}]\text{O}_2//$ hard carbon full cell measured at 52 mA g^{-1} (b) charge-discharge curves of P'2- $\text{K}_{0.83}[\text{Ni}_{0.05}\text{Mn}_{0.95}]\text{O}_2//$ hard carbon full cell measured at 52 mA g^{-1} and (c) the resulting cycling performance between 0.5 and 4.0 V. The full cells were assembled by paired with P'2- $\text{K}_{0.83}[\text{Ni}_{0.05}\text{Mn}_{0.95}]\text{O}_2$ onto Al foil (14ϕ , $\sim 3.0 \text{ mg cm}^{-2}$) and pre-potassiated hard carbon anode onto Cu foil (16ϕ , $\sim 2.3 \text{ mg cm}^{-2}$) for adjusting the N/P capacity ratio of 1.2 in a R2032 coin cell. (For interpretation of the references to color in this figure legend, the reader is referred to the Web version of this article.)

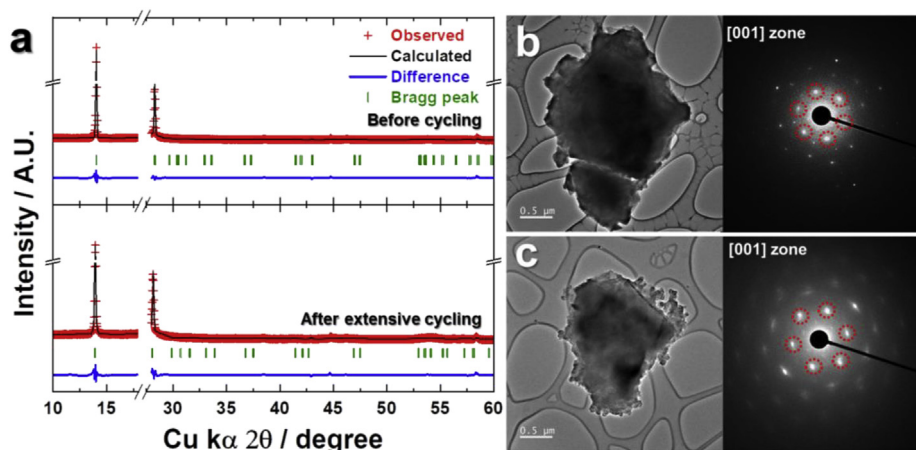


Fig. 8. (a) Rietveld refinement results of XRD data for electrodes before/after extensive cycling; Mylar film: 17° – 30° . Bright-field TEM images for electrodes (b) before cycling and (c) after extensive cycling.

2. Experimental section

2.1. Material preparation

The starting P'2 $\text{Na}_{0.67}[\text{Ni}_{0.05}\text{Mn}_{0.95}]\text{O}_2$ powder was synthesized by spray pyrolysis. The details are provided in our prior work [20–22]. The as-synthesized P'2- $\text{Na}_{0.67}[\text{Ni}_{0.05}\text{Mn}_{0.95}]\text{O}_2$ powder (85 wt%) was blended with a conducting agent (7.5 wt%, Super-P and KS-6 in a weight ratio of 1:1) and polyvinylidene fluoride (PVDF, 7.5 wt%) in *N*-methyl-2-pyrrolidone (NMP). The slurry was applied onto Al foil and dried at 110°C in a vacuum oven. The disc-type electrode (14ϕ , $\sim 3.0 \text{ mg cm}^{-2}$) was first electrochemically desodiated in Na cells, adopting Na metal as an anode in an electrolyte of 0.5 M NaPF_6 in ethylene carbonate (EC) and diethyl carbonate (DEC) (1:1 by volume). Then, potassiation of the desodiated electrode was performed in K cells using K metal as the anode in an electrolyte of 0.5 M KPF_6 in EC:DEC (1:1 by volume) for five cycles in

the voltage range of 1.5–4.3 V. The full cells were assembled by paired with pre-potassiated hard carbon anode (Kureha), which were punched out of the dried electrodes onto Cu foil (16ϕ , $\sim 2.3 \text{ mg cm}^{-2}$). The N/P capacity ratio of 1.2 between anode and cathode was balanced and full cells were separated by a glass fiber (AdvanTec) in a R2032 coin cell.

2.2. Material characterization

X-ray diffraction (XRD; X'Pert, PANalytical) was used to characterize the crystal structures of the as-synthesized P'2- $\text{Na}_{0.67}[\text{Ni}_{0.05}\text{Mn}_{0.95}]\text{O}_2$ and electrochemically produced P'2- $\text{K}_{0.83}[\text{Ni}_{0.05}\text{Mn}_{0.95}]\text{O}_2$ cathode materials. The XRD measurements were performed in the range of 10° – 80° (2θ) with a step size of 0.03° , and the resulting XRD data were refined using the FullProf Rietveld program [28]. The particle morphologies were examined using scanning electron microscopy (SEM; JSM 6400, JEOL) and transmission electron microscopy (TEM; JEM2010, JEOL).

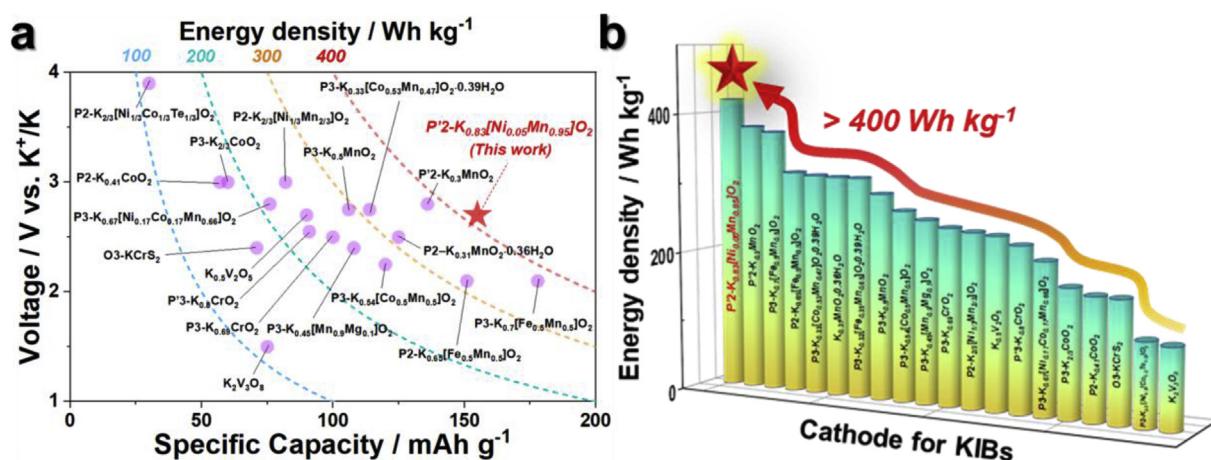


Fig. 9. Comparison of electrochemical performance of reported cathode materials for KIBs; (a) Plots and (b) Bar graph of specific capacity versus operating voltage with calculated energy density curves.

Table 1

Comparison of electrochemical performance of several cathode materials for KIBs.

Material	Voltage/ V vs. K ⁺ / K	Specific capacity/ mAh g ⁻¹	Energy density/ Wh kg ⁻¹	Ref.
P'2-K _{0.83} [Ni _{0.05} Mn _{0.95}]O ₂	1.5–4.3	155	420	Present work
P'2-K _{0.3} MnO ₂	1.5–4.0	136	381	[36]
P3-K _{0.5} MnO ₂	1.5–3.9	106	292	[19]
P2-K _{0.41} CoO ₂	2.0–3.9	57	171	[15]
P3-K _{2/3} CoO ₂	2.0–3.9	60	180	
P3-K _{0.69} CrO ₂	1.5–3.8	100	250	[14]
P'3-K _{0.8} CrO ₂	1.5–3.9	91	232	[39]
K _{0.5} V ₂ O ₅	1.5–3.8	90	243	[54]
K ₂ V ₃ O ₈	1.0–4.2	75	113	[55]
O3-KCrS ₂	1.8–3.0	71	170	[56]
P3-K _{0.54} [Co _{0.5} Mn _{0.5}]O ₂	1.5–3.9	120	270	[16]
P2-K _{2/3} [Ni _{1/3} Mn _{2/3}]O ₂	1.5–4.5	82	246	[23]
P2-K _{0.65} [Fe _{0.5} Mn _{0.5}]O ₂	1.5–4.2	151	317	[40]
P3-K _{0.7} [Fe _{0.5} Mn _{0.5}]O ₂	1.5–4.0	178	374	[17]
P3-K _{0.45} [Mn _{0.9} Mg _{0.1}]O ₂	1.5–4.0	108	259	[41]
P3-K _{0.32} [Fe _{0.35} Mn _{0.65}] O ₂ ·0.39H ₂ O	1.6–3.8	125	313	[42]
K _{0.31} MnO ₂ ·0.36H ₂ O	1.5–4.0	125	313	[57]
P3-K _{0.33} [Co _{0.53} Mn _{0.47}] O ₂ ·0.39H ₂ O	1.6–4.6	114	314	[43]
P3-K _{0.67} [Ni _{0.17} Co _{0.17} Mn _{0.66}] O ₂	2.0–4.3	76	213	[37]
P2-K _{2/3} [Ni _{1/3} Co _{1/3} Te _{1/3}]O ₂	1.25–4.6	30	117	[38]

The chemical compositions of the obtained powders were determined using inductively coupled plasma-atomic emission spectroscopy (ICP-AES; OPTIMA 8300, Perkin-Elmer). Also, the potassium storage mechanism of K_{0.83}[Ni_{0.05}Mn_{0.95}]O₂ was investigated using operando synchrotron XRD (O-SXRD) performed at beamline 3D, and *ex situ* X-ray absorption spectroscopy (XAS) performed at beamline 7D of the Pohang Accelerator Laboratory (PAL), Pohang, South Korea, respectively.

2.3. Computational details

Density functional theory (DFT) calculations were performed using the Vienna *Ab initio* Simulation Package (VASP) [29]. We used projector-augmented wave (PAW) pseudopotentials [30] with a plane-wave basis set as implemented in VASP. Perdew–Burke–Ernzerhof (PBE) parametrization of the generalized gradient approximation (GGA) [31] was used for the exchange–correlation functional. The GGA + U method [32] was adopted to address the localization of the *d*-orbital in

Mn and Ni ions, with U values of 3.9 and 6.0 eV, respectively, as determined in a previous report [33]. For the DFT calculations, a 5 × 3 × 2 k-point grid was used to calculate a 2 × 2 × 1 supercell structure of P'2-K_xMO₂ (M = Mn, Ni). All the calculations were performed with an energy cutoff of 500 eV until the remaining force in the system converged to less than 0.03 eV Å⁻¹ per unit cell. Cluster-assisted statistical mechanics (CASM) software [34] was used to generate all the K/vacancy configurations for each composition. This step was followed by full DFT calculations on a maximum of 30 configurations with the lowest electrostatic energy for each composition to obtain a convex hull plot for P'2-/OP4-K_x[Ni_{0.05}Mn_{0.95}]O₂. Nudged elastic band (NEB) calculations [35] were conducted to determine the activation barrier of K ion diffusion in the P'2-K_x[Ni_{0.05}Mn_{0.95}]O₂ structure. To perform the calculations, five intermediate images were generated between each K site. These structures were then calculated using the NEB algorithm with fixed lattice parameters and free internal atomic positions.

3. Results and discussion

P'2-K_{0.83}[Ni_{0.05}Mn_{0.95}]O₂ was prepared through electrochemical ion exchange of P'2-Na_{0.67}[Ni_{0.05}Mn_{0.95}]O₂. Rietveld refinement of the XRD data (Fig. S1) indicated that the as-synthesized P'2-Na_{0.67}[Ni_{0.05}Mn_{0.95}]O₂ was crystallized into an orthorhombic structure with *Cmcm* space group. As observed in the SEM images in the inset of Fig. S1, the as-synthesized P'2-Na_{0.67}[Ni_{0.05}Mn_{0.95}]O₂ consisted of well-developed crystals with a particle diameter of less than 10 μm. As observed in Fig. 1a, the starting P'2-Na_{0.67}[Ni_{0.05}Mn_{0.95}]O₂ was first subject to cycling in Na cells for 9 cycles to establish Na⁺ diffusion pathways in the structure, and the electrode was recovered after the 10th charge. The original Na_{0.67}[Ni_{0.05}Mn_{0.95}]O₂ was transformed into OP4-Na_{0.12}[Ni_{0.05}Mn_{0.95}]O₂ (Fig. 1b), for which the average oxidation state of Mn was close to Mn⁴⁺ (Fig. 1c). Subsequently, electrochemical potassiation of the desodiated OP4-Na_{0.12}[Ni_{0.05}Mn_{0.95}]O₂ was performed in K cells, with a discharge capacity of 181 mAh g⁻¹ (Fig. 1a) at a slow current rate (26 mA g⁻¹). Chemical analysis using ICP-AES indicated that the composition of the potassiated electrode was K_{0.85}Na_{0.12}[Ni_{0.05}Mn_{0.95}]O₂ (Table S1). K⁺ insertion that lowered the oxidation state of Mn led to the formation of the orthorhombic structure (Fig. 1c), while the Na-containing P'2 phase negligibly remained in the discharged electrode (Fig. 1d). The detection of Na in the TEM-EDS image resulted from the appearance of the Na-based P'2 phase (Fig. 1e).

On the subsequent charge, the potassiated electrode delivered a large charge capacity of approximately 177 mAh g⁻¹ at 52 mA g⁻¹ (Fig. 2a). The higher charge capacity of 12 mAh g⁻¹ may have stemmed from further extraction of remaining sodium ions on the first charge. The

resulting voltage profiles differed from those for Na⁺ de/intercalation, which will be mentioned in Fig. 4. The delivered charge capacities were higher than the capacities obtained on discharge for the initial five cycles, indicating extraction of the remained sodium ion in the structure (Fig. 2a). SEM with EDS mapping images demonstrated that the active materials are composed the K, Mn, Ni, and Na elements (Fig. S2a). Also, the selected-area electron diffraction (SAED) patterns observed along the [110] zone axis for electrode at the 4th cycle confirmed both Na and K phases (Fig. S2b). After five cycles in the K cell, the resulting chemical composition was determined to be K_{0.83}[Ni_{0.05}Mn_{0.95}]O₂ by ICP-AES and sodium element was no longer detectable in the compound. Rietveld refinement of the K_{0.83}[Ni_{0.05}Mn_{0.95}]O₂ electrode showed that the crystal structure was stabilized in the orthorhombic P'2 structure with *Cmcm* space group (Fig. 2b and Table S2), which is the same structure as the starting P'2-Na_{0.67}[Ni_{0.05}Mn_{0.95}]O₂. As mentioned for the ICP-AES data, sodium element was no longer detected in the TEM-EDS analysis (Fig. 2c). To verify the possible K⁺ sites and diffusion pathways in the structure, we performed analyses of the bond-valence-sum (BVS) energy landscape of P'2-K_x[Ni_{0.05}Mn_{0.95}]O₂ using the Bond_Str program in the FullProf package. Fig. 2d shows that there are large two-dimensional spaces for facile diffusion of K⁺ ions between the layers composed of [Ni, Mn]O₆ octahedra along the *ab* plane, which implies facile K⁺ diffusion into P'2-K_x[Ni_{0.05}Mn_{0.95}]O₂ as a cathode material for KIBs. In addition, two possible atomic sites for K⁺ intercalation into the P'2-K_x[Ni_{0.05}Mn_{0.95}]O₂ structure were predicted with Wyckoff positions and atomic coordinates (*x*, *y*, *z*) of 4c (0, -0.067, 0.25) for face-sharing site, K_f(1) and 4c (0, 0.313, 0.25) for edge-sharing site, K_e(2).

After the formation process, P'2-K_{0.83}[Ni_{0.05}Mn_{0.95}]O₂ exhibited stable electrode performance, namely, a high discharge capacity of 155 mAh g⁻¹ (420 Wh kg⁻¹) with capacity retention of ~83% at 52 mA g⁻¹ for 200 cycles (Fig. 3a and b). In particular, the P'2-K_{0.83}[Ni_{0.05}Mn_{0.95}]O₂ electrode delivered a capacity of 78 mAh g⁻¹ at a rate of 1.3 A g⁻¹ (full charge/discharge capacity in 12 min) (Fig. 3c). The long-term cyclability of the material at 520 mA g⁻¹ was further confirmed, as shown in Fig. 3a and b. More than 77% of the initial capacity was maintained for 500 cycles. The superior performance of the present P'2-K_{0.83}[Ni_{0.05}Mn_{0.95}]O₂, compared with that of prismatic site-type (P-type) layered cathode materials such as P2 and P3 types reported in the literature, is worth mentioning [14–17,23,36–43]. Indeed, previously reported P-type layered cathode materials were not able to charge above 4 V in K cells, leading to low Coulombic efficiencies (CEs) of 96%–98% with charge transfer resistance [19]. Because of their undesirable reactions in the high-voltage range, layered oxide cathodes have limitations in terms of delivering high capacities in KIBs. In this work, the resulting CEs were about 99.5% for long-term cycling, as shown in Fig. 3b.

Cathode materials for KIBs are generally exposed in air after synthesis for even short time during transfer from furnace to dry room or glove box. During the exposure in air, adsorption of water molecule is inevitable, so that the surface of active materials is subject to hydration, which may induce unwanted side reaction between electrolyte and K metal. This effect by adsorbed H₂O in the structure usually leads to low Coulombic efficiency when the upper charge cut-off voltage is raised over 4 V at which water molecules decompose [44]. For our case, electrochemical ionic exchange was carried out in Ar-filled glove box, thereby minimizing the influence of moisture. Recent reports on electrochemical-ionic exchange for P3-K_{0.69}CrO₂ [14] and P2-K_{2/3}[Ni_{1/3}Mn_{2/3}]O₂ [23] also showed the good cycling stability with almost 100% Coulombic efficiency even at high charge cutoff voltage of 4.5 V, which is similar to our results.

The outstanding power-capability of P'2-K_{0.83}[Ni_{0.05}Mn_{0.95}]O₂ was also confirmed using the NEB method and first-principles calculation. Fig. 3d shows the motion that theoretically occurs upon K⁺ diffusion along the *bc* plane in the P'2-K_x[Ni_{0.05}Mn_{0.95}]O₂ structure. Along the K₁–K₂ pathway with ~2.96 Å, the predicted activation barrier energy for K⁺ diffusion was only ~271 meV (Fig. 3e). These results indicate the facile K⁺ diffusion in the P'2-K_x[Ni_{0.05}Mn_{0.95}]O₂ structure, which agrees

with the experimentally measured results for the power-capability of P'2-K_{0.83}[Ni_{0.05}Mn_{0.95}]O₂.

Operando synchrotron XRD (O-SXRD) measurements were performed to investigate the K-ion storage mechanism in P'2-K_{0.83}[Ni_{0.05}Mn_{0.95}]O₂ electrode upon charge/discharge at 52 mA g⁻¹ in the voltage range of 1.5–4.3 V (Fig. 4a). During charging, the representative (002), and (118) peaks belonging to the P'2 phase monotonically shifted toward lower angles, and the (114) peak shifted to higher angle in the O-SXRD patterns. Interestingly, as depotassiation progressed, the P'2-K_x[Ni_{0.05}Mn_{0.95}]O₂ phase was retained without phase transition toward OP4 phase, which is different from P'2-Na_{2/3}MnO₂ [20,21]. In case of P'2-Na_{2/3}MnO₂, it was reported that, during charging higher than 4.0V (vs. Na⁺/Na), the P'2 phase almost disappears while a newly formed OP4 phase is formed [45,46]. Moreover, it was also verified that, charging to ~4.3V (vs. K⁺/K), the (002) peak of the P'2 phase slightly shifted toward lower 2θ angles, which indicates increase of *c*-lattice parameter of P'2-K_x[Ni_{0.05}Mn_{0.95}]O₂ that enables maintenance of original P'2 structure. These findings suggest that P'2-K_{0.83}[Ni_{0.05}Mn_{0.95}]O₂ does not experience the phase transition from P'2 to OP4 during depotassiation, which results in the total capacity that cannot exceed 165 mAh g⁻¹, expressed as K_{0.1}[Ni_{0.05}Mn_{0.95}]O₂. On discharge, the peaks corresponding to P'2 phase gradually shifted back to their original peak positions. In addition, the P'2 phase did not evolve toward P2'' at the end of discharge. Indeed, the formation of the P2'' phase is associated with Jahn–Teller distortion, as the P2'' phase was observed when the average oxidation state of Mn was close to 3+ in deeply discharged P2''-Na_{1.0}MnO₂.

Using the detailed structural information, we performed first-principles calculation to predict the theoretical properties and reaction mechanism of P'2-K_x[Ni_{0.05}Mn_{0.95}]O₂. Using CASM software, various K⁺/vacancy configurations for P'2-K_x[Ni_{0.05}Mn_{0.95}]O₂ (0 ≤ *x* ≤ 1) were prepared, and their formation energies were calculated. In addition, as it has been reported in SIBs that the P'2–OP4 phase transition occurs after deintercalation of numerous Na⁺ ions from the structure, we also prepared and calculated the formation energies for various K⁺/vacancy configurations for OP4-K_x[Ni_{0.05}Mn_{0.95}]O₂ (0 ≤ *x* ≤ 0.25). As observed in Fig. 4b, we arranged the formation energies of the various configurations of P'2/OP4-K_x[Ni_{0.05}Mn_{0.95}]O₂ and then calculated the theoretical redox potential of P'2/OP4-K_x[Ni_{0.05}Mn_{0.95}]O₂ during K⁺ de/intercalation using the following equation:

$$V = - \frac{E[\text{K}_{x_2}\text{Ni}_{0.05}\text{Mn}_{0.95}\text{O}_2] - E[\text{K}_{x_1}\text{Ni}_{0.05}\text{Mn}_{0.95}\text{O}_2] - (x_2 - x_1)E[\text{K}]}{(x_2 - x_1)F}, \quad (1)$$

where *V* is the average redox potential of P'2/OP4-K_x[Ni_{0.05}Mn_{0.95}]O₂ depending on the K content (x₁ ≤ *x* ≤ x₂), and E[K_xNi_{0.05}Mn_{0.95}O₂] is the most stable formation energy for the composition P'2/OP4-K_x[Ni_{0.05}Mn_{0.95}]O₂. As observed in Fig. 4c, the predicted redox potentials of P'2-K_x[Ni_{0.05}Mn_{0.95}]O₂ agreed with the experimentally measured charge/discharge curves, and it was verified that P'2-K_x[Ni_{0.05}Mn_{0.95}]O₂ can exhibit an exceptionally large specific capacity of ~160 mAh g⁻¹, corresponding to ~0.75 mol K⁺ de/intercalation. These results are consistent with the experimental results shown in Fig. 3.

Particularly, it was predicted that, although all of the K⁺ ions are deintercalated from the structure, the P'2-K_x[Ni_{0.05}Mn_{0.95}]O₂ phases (0 ≤ *x* ≤ 0.25) are more stable than OP4-K_x[Ni_{0.05}Mn_{0.95}]O₂ (0 ≤ *x* ≤ 0.25) (Fig. 4b). This prediction implies that P'2-K_x[Ni_{0.05}Mn_{0.95}]O₂, which is free from the P'2–OP4 phase transition, may not experience a large volume change during charge/discharge. This may be responsible for the outstanding electrochemical performance of P'2-K_x[Ni_{0.05}Mn_{0.95}]O₂ as a cathode for KIBs. It is thought that the absence of the P'2–OP4 phase transition in P'2-K_x[Ni_{0.05}Mn_{0.95}]O₂, unlike P'2-Na_xMO₂, may be attributed to the size difference of the required space between prismatic sites for K⁺ and Na⁺. Because of the larger size of K⁺ ions relative to that of Na⁺ ions, K⁺ ions should require larger prismatic sites than Na⁺ ions, as confirmed by first-principles calculation comparing the prismatic sites of

P'2-K₁[Ni_{0.05}Mn_{0.95}]O₂ and P'2-Na₁[Ni_{0.05}Mn_{0.95}]O₂ (Fig. S3). These results imply that the minimum K⁺ slab distance for P'2-K_x[Ni_{0.05}Mn_{0.95}]O₂ should be larger than that of Na⁺ for P'2-Na_xMO₂. As mentioned in Fig. 2a, there was appearance of a voltage plateau at around 3.65 V on discharge for the early stage of electrochemical ion exchange when sodium ions were remained in the crystal structure. However, the plateau was not observed in the P'2-K_x[Ni_{0.05}Mn_{0.95}]O₂ after completion of the ion exchange. It is thought that the difference is ascribed to the insertion of the potassium ions into the OP4 structure in which sodium ions were remained in the crystal structure that prefers to stabilize as OP4 structure at desodiated state.

Our *o*-SXR and first principles calculation demonstrated absence of the P'2 to OP4 phase transition but the occurrence of the single phase reaction in P'2-K_x[Ni_{0.05}Mn_{0.95}]O₂; however, the mentioned phase transition is typical in P'2-Na₁MO₂ structure [M = Mn, Fe, Co, Ni, and Al] [20]. Indeed, the phase transition from P'2 phase to OP4 phase is associated with the large decrease in the interlayer distance below the certain value (~5.19 Å), when a large amount of sodium ions over 0.75 mol are deintercalated from P'2-Na₁MO₂ structure [20]. This implies that the interslab distance for the P'2-K_x[Ni_{0.05}Mn_{0.95}]O₂ should be also lowered than ~5.19 Å to induce the P'2-OP4 phase transition by depotassiation. However, such reduction in the interslab distance did not occur in both experimental and simulated results, while the interslab distance increased as depotassiation progressed (Fig. 5a and b). In consideration of the large prismatic size of KO₆ (~3.82 Å) relative to NaO₆ (~3.22 Å) (Fig. S3), when the large potassium ions are remained in the crystal structure, the interslab distance for the P'2-K_x[Ni_{0.05}Mn_{0.95}]O₂ is larger than that for the P'2-Na_xMO₂ at the same compositions of K and Na (Fig. 5c and d). This limitation in the variation in the interslab, therefore, is likely to induce the single phase reaction for the P'2-K_x[Ni_{0.05}Mn_{0.95}]O₂. We further compared the interslab distances between P'2-K_x[Ni_{0.05}Mn_{0.95}]O₂ (x = 0.1, 0.5, 0.83) and P'2-Na_x[Ni_{0.05}Mn_{0.95}]O₂ (x = 0.1, 0.5, 0.83) [20] (Fig. 5c and d), which validates that the presence of potassium ions in the prismatic sites for the P'2-K_x[Ni_{0.05}Mn_{0.95}]O₂ resulted in the less change in the interslab distance relative to that of sodium ions in P'2-Na_x[Ni_{0.05}Mn_{0.95}]O₂ due to the large size of potassium ions. With K⁺ deintercalation from the structure, the K⁺ slab distance of P'2-K_x[Ni_{0.05}Mn_{0.95}]O₂ monotonously increased, resulting from repulsion between oxygen ions (O²⁻-O²⁻) along the *c*-axis (Fig. 5a and b). Therefore, the absence of the P'2-OP4 phase transition at P'2-K_x[Ni_{0.05}Mn_{0.95}]O₂ can be explained by less structural change by the presence of large potassium in the prismatic site of the P'2-K_{0.25}[Ni_{0.05}Mn_{0.95}]O₂ structure.

As K⁺ deintercalation was progressed, the K⁺ slab distance of P'2-K_x[Ni_{0.05}Mn_{0.95}]O₂ monotonously increased, because ionic character presenting between interlayers is predominant between oxygen ions (O²⁻-O²⁻) along the *c*-axis. However, the interslab distance of 6.4 Å for the P'2-K_{0.1}[Ni_{0.05}Mn_{0.95}]O₂ was dramatically reduced to 4.97 Å for the simulated P'2-K₀[Ni_{0.05}Mn_{0.95}]O₂ in Fig. 5a, which result from that covalent character presenting between transition metal and oxygen is favored for the deeply depotassiated state. This tendency is frequently observed in layered compounds [20,21]. As seen in Fig. 5b, the interslab distance predicted by first principles calculation was approximately 6.4 Å for the P'2-K_{0.1}[Ni_{0.05}Mn_{0.95}]O₂. However, the average interslab distance was calculated to be 4.97 Å for the P'2-K₀[Ni_{0.05}Mn_{0.95}]O₂ in Fig. 5a. The full depotassiation resulted in the abrupt contraction of the interslab distance in the structure, which may not be favored to retain the crystal structure.

Furthermore, we verified, through TEM-EDS and ICP analyses (Fig. S4), that the atomic ratio between K, Ni and Mn at the P'2-K_x[Ni_{0.05}Mn_{0.95}]O₂ electrode charged to 4.3V (vs. K⁺/K) is approximately 0.105 : 0.051 : 0.949. It was reported that P'2-OP4 phase transition is occurred when the Na contents in P'2-Na_xMnO₂ is lowered to less than ~0.25 mol [47]. However, although K contents in P'2-K_x[Ni_{0.05}Mn_{0.95}]O₂ was lowered below ~0.25 mol, the P'2 phase is retained without P'2-OP4 phase transition, which supports the results of

first principles calculation and O-SXRD.

During charge/discharge, the XRD peaks for P'2-K_x[Ni_{0.05}Mn_{0.95}]O₂ continuously shifted, and the crystal structure was retained without phase transition, indicating a single-phase reaction of P'2-K_x[Ni_{0.05}Mn_{0.95}]O₂ during K⁺ de/intercalation. In addition, we compared the predicted structural change of the K⁺ slab distance of P'2-K_x[Ni_{0.05}Mn_{0.95}]O₂ as a function of the K⁺ content with the experimental results verified through O-SXRD (Fig. 5b), which indicated that the predicted structural change of P'2-K_x[Ni_{0.05}Mn_{0.95}]O₂ was consistent with the experimental results. Specifically, the total volume change of P'2-K_x[Ni_{0.05}Mn_{0.95}]O₂ during charge/discharge was confirmed to be only ~5.9%, which may contribute to the outstanding cycle performance of P'2-K_{0.83}[Ni_{0.05}Mn_{0.95}]O₂ as a promising cathode for KIBs.

X-ray absorption near-edge structure (XANES) analysis was performed during de/potassiation. Compared with the reference spectra of Mn³⁺₂O₃, Mn⁴⁺O₂, and Ni²⁺O, de/potassiation induced a shift of the Mn and Ni K-edge spectra toward higher or lower photon energy, suggesting that both Mn and Ni ions are involved in the redox reaction (Fig. 6a and b). The Mn oxidation state of K_x[Ni_{0.05}Mn_{0.95}]O₂ (x = 0.10) shifted toward Mn⁴⁺ on charge, whereas the Mn oxidation state of K_x[Ni_{0.05}Mn_{0.95}]O₂ (x = 0.83, ~3.25+) was slightly higher than that of Mn³⁺₂O₃, suggesting less dominance by the Jahn–Teller distortion by Mn³⁺. The Ni K-edge spectrum of K_{0.83}[Ni_{0.05}Mn_{0.95}]O₂ was similar to that of NiO (Fig. 6b), indicating that the oxidation state of Ni was 2+. Compared with that of the fresh state, the Ni K-edge spectrum of K_{0.10}[Ni_{0.05}Mn_{0.95}]O₂ shifted toward higher energy after charge to 4.3 V because of the oxidation of Ni²⁺ to Ni³⁺; in addition, the reverse was observed for K_{0.83}[Ni_{0.05}Mn_{0.95}]O₂ on discharge, verifying the reversibility contributed by the Ni^{3+/2+} redox pair during the K⁺ ion storage reaction. As shown in Fig. 6c, the integrated spin moments of Mn and Ni ions in P'2-K₁[Ni_{0.05}Mn_{0.95}]O₂ were verified to be approximately three and one, respectively, and after K⁺ deintercalation from P'2-K_x[Ni_{0.05}Mn_{0.95}]O₂, they increased to four and two, respectively. These results indicate the occurrence of Mn³⁺/Mn⁴⁺ and Ni²⁺/Ni³⁺ redox reactions for P'2-K_x[Ni_{0.05}Mn_{0.95}]O₂ during charge/discharge. In addition, it was verified that the Ni²⁺/Ni³⁺ redox reaction in P'2-K_x[Ni_{0.05}Mn_{0.95}]O₂ occurred during the initial K⁺ deintercalation from P'2-K₁[Ni_{0.05}Mn_{0.95}]O₂ to P'2-K_{0.75}[Ni_{0.05}Mn_{0.95}]O₂ in the low-operation-voltage range. These computational results are consistent with the experimentally obtained XANES results.

Graphitic carbon, MoSe₂, and (Bi,Sb)₂S₃ have been investigated as anode materials for KIBs [48–50]. Also, carbon-based anode materials such as graphite and hard carbon, are widely applicable due to storage ability of potassium ions [51,52]. We obtained better results for hard carbon rather than graphite in our testing condition, delivering a reasonable capacity of ~250 mAh g⁻¹ with good cyclability (Fig. S5). For the reason, the hard carbon was chosen as the anode material for fabrication of full cells in this work [16,53]. We fabricated the full cell paired with hard carbon anode after adjusting the N/P capacity ratio of 1.2 for minimizing the irreversibility at the first cycle (formation and grading after five cycles) and the formation of a solid electrolyte interphase (SEI) layer on the surface of the hard carbon anode (Fig. 7a). Surprisingly, the P'2-K_{0.83}[Ni_{0.05}Mn_{0.95}]O₂ full cell delivered an unexpectedly high capacity of 135 mAh g⁻¹ (283 Wh kg⁻¹) in the voltage range of 0.5–4.0 V (Fig. 7b and c), compared with reported values in literature for KIBs. Furthermore, the results revealed the outstanding long-term cyclability, providing capacity retention of ~80% after 300 cycles, which indicates its excellent structural stability (Fig. 7b and c). Our findings indicate that the present P'2-type K_{0.83}[Ni_{0.05}Mn_{0.95}]O₂ is a promising material for the development of energy storage systems requiring high power capability with long-term cyclability.

The structural stability of P'2-K_{0.83}[Ni_{0.05}Mn_{0.95}]O₂ was investigated using *ex situ* XRD and TEM analyses of electrodes before/after extensive cycling (Fig. 8). Compared with the electrode before cycling, the electrode after extensive cycling retained its high crystallinity without impurities even after 500 cycles. The sharp feature of the (002) and (004)

peaks for the P'2 phase still remained (Fig. 8a), and the variation in the lattice parameters was also slight for the a , b , and c -axes, with $\Delta a = 0.0534 \text{ \AA}$, $\Delta b = 0.0542 \text{ \AA}$, and $\Delta c = 0.0684 \text{ \AA}$ (Table S3). Note that the post-cycled P'2-type $\text{K}_{0.83}[\text{Ni}_{0.05}\text{Mn}_{0.95}]\text{O}_2$ retained its structural integrity, leading to long-term cyclability with capacity retention of $\sim 77\%$ for 500 cycles (Fig. 3b). To further confirm the structural stability, TEM analysis of electrodes before/after extensive cycling was conducted. The post-cycled electrode was able to maintain the original morphology of the pre-cycled electrode without morphological degradation after 500 cycles (Fig. 8b and c). Compared with the results reported in the literature, the electrochemical performance of the present P'2- $\text{K}_{0.83}[\text{Ni}_{0.05}\text{Mn}_{0.95}]\text{O}_2$ is one of the best outputs among existing cathode materials for KIBs, as illustrated in Fig. 9 and Table 1.

4. Conclusion

In summary, P'2- $\text{K}_{0.83}[\text{Ni}_{0.05}\text{Mn}_{0.95}]\text{O}_2$, electrochemically prepared using Na/K ion exchange from desodiated $\text{OP4-Na}_x[\text{Ni}_{0.05}\text{Mn}_{0.95}]\text{O}_2$ in K cells, is investigated for use as a high-energy-density cathode for KIBs. The P'2- $\text{K}_{0.83}[\text{Ni}_{0.05}\text{Mn}_{0.95}]\text{O}_2$ electrode delivers an unexpectedly high power capability of $\sim 155 \text{ mAh g}^{-1}$ and a high energy density of $\sim 420 \text{ Wh kg}^{-1}$ in the voltage range of 1.5–4.3 V. According to experimental and theoretical investigations, the potassium storage mechanism in $\text{K}_x[\text{Ni}_{0.05}\text{Mn}_{0.95}]\text{O}_2$ is progressed via a single-phase reaction maintaining the P'2 phase. Furthermore, the facile K^+ migration in the $\text{K}_x[\text{Ni}_{0.05}\text{Mn}_{0.95}]\text{O}_2$ structure with a low activation barrier energy of $\sim 271 \text{ meV}$ enabled achievement of high power-capability. Full cell paired with hard carbon anode results in high energy density of 283 Wh kg^{-1} in the voltage range of 0.5–4.0 V as well as good capacity retention for long term cycles. These results indicate that the present P'2-type $\text{K}_{0.83}[\text{Ni}_{0.05}\text{Mn}_{0.95}]\text{O}_2$ is one of the candidates for high-energy-density cathodes for KIBs.

Declaration of competing interest

The authors declare that they have no known competing financial interests or personal relationships that could have appeared to influence the work reported in this paper.

Acknowledgements

This research was supported by the Basic Science Research Program through the National Research Foundation funded by the Ministry of Science and ICT of Korea (NRF-2015M3D1A1069713, NRF-2017R1A2A2A05069634, and NRF-2019H1D8A2106002).

Appendix A. Supplementary data

Supplementary data to this article can be found online at <https://doi.org/10.1016/j.ensm.2020.02.025>.

References

- B. Dunn, H. Kamath, J.-M. Tarascon, Electrical energy storage for the grid: a battery of choices, *Science* 334 (2011) 928–935, <https://doi.org/10.1126/science.1212741>.
- H. Zhang, X.P. Gao, G.R. Li, T.Y. Yan, H.Y. Zhu, Electrochemical lithium storage of sodium titanate nanotubes and nanorods, *Electrochim. Acta* 53 (2008) 7061–7068, <https://doi.org/10.1016/j.electacta.2008.05.036>.
- J.-Y. Hwang, S.-T. Myung, Y.-K. Sun, Sodium-ion batteries: present and future, *Chem. Soc. Rev.* 46 (2017) 3529–3614, <https://doi.org/10.1039/C6CS00776G>.
- I. Sultana, T. Ramireddy, M.M. Rahman, Y. Chen, A.M. Glushenkov, Tin-based composite anodes for potassium-ion batteries, *Chem. Commun.* 52 (2016) 9279–9282, <https://doi.org/10.1039/C6CC03649J>.
- C.D. Wessells, S.V. Peddada, R.A. Huggins, Y. Cui, Nickel hexacyanoferrate nanoparticle electrodes for aqueous sodium and potassium ion batteries, *Nano Lett.* 11 (2011) 5421–5425, <https://doi.org/10.1021/nl203193q>.
- V. Palomares, M. Casas-Cabanas, E. Castillo-Martinez, M.H. Han, T. Rojo, Update on Na-based battery materials. A growing research path, *Energy Environ. Sci.* 6 (2013) 2312–2337, <https://doi.org/10.1039/C3EE41031E>.
- A. Eftekhari, Potassium secondary cell based on prussian blue cathode, *J. Power Sources* 126 (2004) 221–228, <https://doi.org/10.1016/j.jpowsour.2003.08.007>.
- C. Zhang, Y. Xu, M. Zhou, L. Liang, H. Dong, M. Wu, Y. Yang, Y. Lei, Batteries: potassium prussian blue nanoparticles: a low-cost cathode material for potassium-ion batteries, *Adv. Funct. Mater.* 27 (2017), <https://doi.org/10.1002/adfm.201770024>.
- J.-Y. Hwang, S.-T. Myung, Y.-K. Sun, Recent progress in rechargeable potassium batteries, *Adv. Funct. Mater.* 28 (2018), 1802938, <https://doi.org/10.1002/adfm.201802938>.
- K. Chihara, A. Katogi, K. Kubota, S. Komaba, KVPO_4F and KVPO_4 toward 4 volt-class potassium-ion batteries, *Chem. Commun.* 53 (2017) 5208–5211, <https://doi.org/10.1039/C6CC10280H>.
- X. Wang, C. Niu, J. Meng, P. Hu, X. Xu, X. Wei, L. Zhou, K. Zhao, W. Luo, M. Yan, L. Mai, Sodium-ion batteries: novel $\text{K}_3\text{V}_2(\text{PO}_4)_3/\text{C}$ bundled nanowires as superior sodium-ion battery electrode with ultrahigh cycling stability, *Adv. Energy Mater.* 5 (2015), 1500716, <https://doi.org/10.1002/aenm.201570091>.
- A. Wild, M. Strumpf, B. Häupler, M.D. Hager, U.S. Schubert, All-organic battery composed of thianthrene- and TCAQ-based polymers, *Adv. Energy Mater.* 7 (2017), 1601415, <https://doi.org/10.1002/aenm.201601415>.
- Q. Zhao, J. Wang, Y. Lu, Y. Li, G. Liang, J. Chen, Oxocarbon salts for fast rechargeable batteries, *Angew. Chem. Int. Ed.* 55 (2016) 12528–12532, <https://doi.org/10.1002/anie.201607194>.
- J.-Y. Hwang, J. Kim, T.-Y. Yu, S.-T. Myung, Y.-K. Sun, Development of P3- $\text{K}_{0.69}\text{CrO}_2$ as an ultra-high-performance cathode material for K-ion batteries, *Energy Environ. Sci.* 11 (2018) 2821–2827, <https://doi.org/10.1039/c8ee01365a>.
- Y. Hironaka, K. Kubota, S. Komaba, P2- and P3- K_xCoO_2 as an electrochemical potassium intercalation host, *Chem. Commun.* 53 (2017) 3693–3696, <https://doi.org/10.1039/C7CC00806F>.
- J.U. Choi, J. Kim, J.-Y. Hwang, J.H. Jo, Y.-K. Sun, S.-T. Myung, $\text{K}_{0.54}[\text{Co}_{0.5}\text{Mn}_{0.5}]\text{O}_2$: new cathode with high power capability for potassium-ion batteries, *Nano Energy* 61 (2019) 284–294, <https://doi.org/10.1016/j.nanoen.2019.04.062>.
- X. Wang, X. Xu, C. Niu, J. Meng, M. Huang, X. Liu, Z. Liu, L. Mai, Earth abundant Fe/Mn-based layered oxide interconnected nanowires for advanced K-ion full batteries, *Nano Lett.* 17 (2017) 544–550, <https://doi.org/10.1021/acs.nanolett.6b04611>.
- J. Han, G.-N. Li, F. Liu, M. Wang, Y. Zhang, L. Hu, C. Dai, M. Xu, Investigation of $\text{K}_3\text{V}_2(\text{PO}_4)_3/\text{C}$ nanocomposites as high-potential cathode materials for potassium-ion batteries, *Chem. Commun.* 53 (2017) 1805–1808, <https://doi.org/10.1039/C6CC10065A>.
- H. Kim, D.-H. Seo, J.C. Kim, S.-H. Bo, L. Liu, T. Shi, G. Ceder, Investigation of potassium storage in layered P3-Type $\text{K}_{0.5}\text{MnO}_2$ cathode, *Adv. Mater.* 29 (2017), 1702480, <https://doi.org/10.1002/adma.201702480>.
- J.U. Choi, C.S. Yoon, Q. Zhang, P. Kaghazchi, Y.H. Jung, K.-S. Lee, D.-C. Ahn, Y.-K. Sun, S.-T. Myung, Understanding on the structural and electrochemical performance of orthorhombic sodium manganese oxides, *J. Mater. Chem.* 7 (2019) 202–211, <https://doi.org/10.1039/C8TA08796B>.
- J.U. Choi, Y.J. Park, J.H. Jo, L.-Y. Kuo, P. Kaghazchi, S.-T. Myung, Unraveling the role of earth-abundant Fe in the suppression of jahn-teller distortion of P'2-Type $\text{Na}_{2/3}\text{MnO}_2$: experimental and theoretical studies, *ACS Appl. Mater. Interfaces* 10 (2018) 40978–40984, <https://doi.org/10.1021/acsami.8b16522>.
- Y.J. Park, J.U. Choi, J.H. Jo, C.-H. Jo, J. Kim, S.-T. Myung, A new strategy to build a high-performance P'2-type cathode material through titanium doping for sodium-ion batteries, *Adv. Funct. Mater.* (2019), 1901912, <https://doi.org/10.1002/adfm.201901912>.
- M.G.T. Nathan, N. Naveen, W.B. Park, K.-S. Sohn, M. Pyo, Fast chargeable P2- $\text{K}_{0.2/3}[\text{Ni}_{1/3}\text{Mn}_{2/3}]\text{O}_2$ for potassium ion battery cathodes, *J. Power Sources* 438 (2019), 226992, <https://doi.org/10.1016/j.jpowsour.2019.226992>.
- W.A. Herrmann, *Synthetic Methods of Organometallic and Inorganic Chemistry*, 1996, <https://doi.org/10.1055/b-0035-108134>.
- L. Xue, H. Gao, Y. Li, J.B. Goodenough, Cathode dependence of liquid-alloy Na-K anodes, *J. Am. Chem. Soc.* 140 (2018) 3292–3298, <https://doi.org/10.1021/jacs.7b12267>.
- L. Zhang, X. Xia, Y. Zhong, D. Xie, S. Liu, X. Wang, J. Tu, Exploring self-healing liquid Na-K alloy for dendrite-free electrochemical energy storage, *Adv. Mater.* 30 (2018), 1804011, <https://doi.org/10.1002/adma.201804011>.
- H. Euchner, O. Clemens, M.A. Reddy, Unlocking the potential of weberite-type metal fluorides in electrochemical energy storage, *NPJ Comput. Mater.* 5 (2019) 31, <https://doi.org/10.1038/s41524-019-0166-3>.
- J. Carvajal, *Abstracts of the Satellite Meeting on Powder Diffraction of the XV Congress of the IUCr*, 1990.
- G. Kresse, J. Furthmüller, Efficiency of ab-initio total energy calculations for metals and semiconductors using a plane-wave basis set, *Comput. Mater. Sci.* 6 (1996) 15–50, [https://doi.org/10.1016/0927-0256\(96\)00008-0](https://doi.org/10.1016/0927-0256(96)00008-0).
- P.E. Blöchl, Projector augmented-wave method, *Phys. Rev. B* 50 (1994) 17953–17979.
- J.P. Perdew, K. Burke, M. Ernzerhof, Generalized gradient approximation made simple, *Phys. Rev. Lett.* 77 (1996) 3865–3868, <https://doi.org/10.1103/PhysRevB.50.17953>.
- I.A. Vladimir, F. Aryasetiawan, A.I. Lichtenstein, First-principles calculations of the electronic structure and spectra of strongly correlated systems: the LDA+U method, *J. Phys. Condens. Matter* 9 (1995) 106–116, <https://doi.org/10.1088/0953-8984/9/4/002>.
- A. Jain, G. Hautier, S.P. Ong, C.J. Moore, C.G. Fischer, K.A. Persson, G. Ceder, Formation enthalpies by mixing GGA and GGA+U calculations, *Phys. Rev. B* 84 (2011), 045115, <https://doi.org/10.1103/PhysRevB.84.045115>.

- [34] A.V.d. Ven, J.C. Thomas, Q. Xu, J. Bhattacharya, Linking the electronic structure of solids to their thermodynamic and kinetic properties, *J. Mat.* 80 (2010) 1393–1410, <https://doi.org/10.1016/j.matcom.2009.08.008>.
- [35] G. Henkelman, B.P. Uberuaga, H. Jónsson, A climbing image nudged elastic band method for finding saddle points and minimum energy paths, *J. Chem. Phys.* 113 (2000) 9901–9904, <https://doi.org/10.1063/1.1329672>.
- [36] C. Vaalma, G.A. Giffin, D. Buchholz, S. Passerini, Non-aqueous K-ion battery based on layered $K_{0.3}MnO_2$ and hard carbon/carbon black, *J. Electrochem. Soc.* 163 (2016) A1295–A1299, <https://doi.org/10.1149/2.0921607jes>.
- [37] C. Liu, S. Luo, H. Huang, Z. Wang, A. Hao, Y. Zhai, Z. Wang, $K_{0.67}Ni_{0.17}Co_{0.17}Mn_{0.66}O_2$: a cathode material for potassium-ion battery, *Electrochem. Commun.* 82 (2017) 150–154, <https://doi.org/10.1016/j.elecom.2017.08.008>.
- [38] T. Masese, K. Yoshii, M. Kato, K. Kubota, Z.-D. Huang, H. Senoh, M. Shikano, A high voltage honeycomb layered cathode framework for rechargeable potassium-ion battery: P2-type $K_{2/3}Ni_{1/3}Co_{1/3}Te_{1/3}O_2$, *Chem. Commun.* 55 (2019) 985–988, <https://doi.org/10.1039/C8CC07239F>.
- [39] N. Naveen, S.C. Han, S.P. Singh, D. Ahn, K.-S. Sohn, M. Pyo, Highly stable P'3- $K_{0.8}CrO_2$ cathode with limited dimensional changes for potassium ion batteries, *J. Power Sources* 430 (2019) 137–144, <https://doi.org/10.1016/j.jpowsour.2019.05.017>.
- [40] T. Deng, X. Fan, J. Chen, L. Chen, C. Luo, X. Zhou, J. Yang, S. Zheng, C. Wang, Layered P2-type $K_{0.65}Fe_{0.5}Mn_{0.5}O_2$ microspheres as superior cathode for high-energy potassium-ion batteries, *Adv. Funct. Mater.* 28 (2018), 1800219, <https://doi.org/10.1002/adfm.201800219>.
- [41] C.-L. Liu, S.-H. Luo, H.-B. Huang, Y.-C. Zhai, Z.-W. Wang, Low-cost layered $K_{0.45}Mn_{0.9}Mg_{0.1}O_2$ as a high-performance cathode material for K-ion batteries, *ChemElectroChem* 6 (2019) 2308–2315, <https://doi.org/10.1002/celec.201900326>.
- [42] S. Wang, Y.-H. Zhu, J.-M. Yan, X.-B. Zhang, P3-type $K_{0.32}Fe_{0.35}Mn_{0.65}O_2 \cdot 0.39H_2O$: a promising cathode for Na-ion full batteries, *J. Mater. Chem.* 6 (2018) 13075–13081, <https://doi.org/10.1039/C8TA03270J>.
- [43] S. Wang, T. Sun, S. Yuan, Y.-H. Zhu, X.-B. Zhang, J.-M. Yan, Q. Jiang, P3-type $K_{0.33}Co_{0.53}Mn_{0.47}O_2 \cdot 0.39H_2O$: a novel bifunctional electrode for Na-ion batteries, *Mater. Horiz.* 4 (2017) 1122–1127, <https://doi.org/10.1039/C7MH00512A>.
- [44] J.H. Jo, J.-Y. Hwang, J.U. Choi, Y.-K. Sun, S.-T. Myung, Layered $K_{0.28}MnO_2 \cdot 0.15H_2O$ as a cathode material for potassium-ion intercalation, *ACS Appl. Mater. Interfaces* 11 (2019) 43312–43319, <https://doi.org/10.1021/acsaami.9b18540>.
- [45] G. Singh, J.M. López del Amo, M. Galceran, S. Pérez-Villar, T. Rojo, Structural evolution during sodium deintercalation/intercalation in $Na_{2/3}[Fe_{1/2}Mn_{1/2}]O_2$, *J. Mater. Chem.* 3 (2015) 6954–6961, <https://doi.org/10.1039/C4TA06360K>.
- [46] N. Yabuuchi, M. Kajiyama, J. Iwatate, H. Nishikawa, S. Hitomi, R. Okuyama, R. Usui, Y. Yamada, S. Komaba, P2-type $Na_x[Fe_{1/2}Mn_{1/2}]O_2$ made from earth-abundant elements for rechargeable Na batteries, *Nat. Mater.* 11 (2012) 512–517, <https://doi.org/10.1038/nmat3309>.
- [47] S. Kumakura, Y. Tahara, K. Kubota, K. Chihara, S. Komaba, Sodium and manganese stoichiometry of P2-Type $Na_{2/3}MnO_2$, *Angew. Chem. Int. Ed.* 55 (2016) 12760–12763, <https://doi.org/10.1002/anie.201606415>.
- [48] Z. Liu, J. Wang, X. Jia, W. Li, Q. Zhang, L. Fan, H. Ding, H. Yang, X. Yu, X. Li, B. Lu, Graphene armored with a crystal carbon shell for ultrahigh-performance potassium ion batteries and aluminum batteries, *ACS Nano* 13 (2019) 10631–10642, <https://doi.org/10.1021/acsnano.9b04893>.
- [49] J. Ge, L. Fan, J. Wang, Q. Zhang, Z. Liu, E. Zhang, Q. Liu, X. Yu, B. Lu, $MoSe_2$ /N-doped carbon as anodes for potassium-ion batteries, *Adv. Energy Mater.* 8 (2018), 1801477, <https://doi.org/10.1002/aenm.201801477>.
- [50] J. Wang, L. Fan, Z. Liu, S. Chen, Q. Zhang, L. Wang, H. Yang, X. Yu, B. Lu, In situ alloying strategy for exceptional potassium ion batteries, *ACS Nano* 13 (2019) 3703–3713, <https://doi.org/10.1021/acsnano.9b00634>.
- [51] L. Fan, R. Ma, Q. Zhang, X. Jia, B. Lu, Graphite anode for a potassium-ion battery with unprecedented performance, *Angew. Chem. Int. Ed.* 131 (2019) 10610–10615, <https://doi.org/10.1002/ange.201904258>.
- [52] Z. Jian, Z. Xing, C. Bommier, Z. Li, X. Ji, Hard carbon microspheres: potassium-ion anode versus sodium-ion anode, *Adv. Energy Mater.* 6 (2016), 1501874, <https://doi.org/10.1002/aenm.201501874>.
- [53] J.U. Choi, J. Kim, J.H. Jo, H.J. Kim, Y.H. Jung, D.-C. Ahn, Y.-K. Sun, S.-T. Myung, Facile migration of potassium ions in a ternary P3-type $K_{0.5}[Mn_{0.8}Fe_{0.1}Ni_{0.1}]O_2$ cathode in rechargeable potassium batteries, *Energy Storage Mater.* (2019), <https://doi.org/10.1016/j.ensm.2019.09.015> online 12.
- [54] L. Deng, X. Niu, G. Ma, Z. Yang, L. Zeng, Y. Zhu, L. Guo, Layered potassium vanadate $K_{0.5}V_2O_5$ as a cathode material for nonaqueous potassium ion batteries, *Adv. Funct. Mater.* 28 (2018), 1800670, <https://doi.org/10.1002/adfm.201800670>.
- [55] J.H. Jo, J.-Y. Hwang, J.U. Choi, H.J. Kim, Y.-K. Sun, S.-T. Myung, Potassium vanadate as a new cathode material for potassium-ion batteries, *J. Power Sources* 432 (2019) 24–29, <https://doi.org/10.1016/j.jpowsour.2019.05.064>.
- [56] N. Naveen, W.B. Park, S.P. Singh, S.C. Han, D. Ahn, K.-S. Sohn, M. Pyo, $KCrS_2$ cathode with considerable cyclability and high rate performance: the first K^+ stoichiometric layered compound for potassium-ion batteries, *Small* 14 (2018), 1803495, <https://doi.org/10.1002/smll.201803495>.
- [57] A. Gao, M. Li, N. Guo, D. Qiu, Y. Li, S. Wang, X. Lu, F. Wang, R. Yang, K-birnessite electrode obtained by ion exchange for potassium-ion batteries: insight into the concerted ionic diffusion and K storage mechanism, *Adv. Energy Mater.* 9 (2019), 1802739, <https://doi.org/10.1002/aenm.201802739>.